Microscopic investigations into fission dynamics beyond the saddle point

Liang Tong and Shiwei Yan[*]

Department of Physics, Beijing Normal University, Beijing 100875, China

The real-space density-constrained time-dependent Hartree-Fock-Bogoliubov method is exploited to obtain the dynamic potential energy and several experimental variables of fission fragments. The resultant predictions of collective variables, especially the total kinetic energy and total excitation energy of the fission fragments, finely match the experimental data. It is demonstrated that scission dynamics including the shell effects and pairing correlations should be the focus of further studies.

I. INTRODUCTION

The understanding of the nuclear fission phenomena has been a crucial problem in the fundamental science of nuclear physics over the past eighty years. Huge efforts have been pursued by several generations of physicists and the great progress has been made by both the experimental and theoretical studies. However, many crucial facets of the fission process are not understood at a fundamental level and still represent one of the most challenging problems in nuclear science for further explorations [1–6].

From a theoretical point of view, starting from Bohr and Wheeler's seminal paper written in 1939 [7], nuclear fission is considered as an adiabatic process and thus the adiabatic approximation is extensively used to describe the fission from the compound states of fissioning nuclei up to the scission, and even the formations of the fragments. Within adiabatic approximation, the nucleonic degrees of freedom are fully equilibrated while the system evolves over a potential-energy surface (PES) defined by the macroscopic degrees of freedom such as elongation and mass asymmetry. Under the adiabatic approximation, various versions of the macroscopic-microscopic (MM) model [8–10], the stochastic dynamics model [11–15], the time-dependent generator coordinate method (TDGCM) [16–19] and the adiabatic time-dependent Hartree-Fock (ATDHF) theory [20–23] have been proposed and the considerable progresses have been made with them.

Consider that the minimum average timescale for fission process is of the order of $(20$–$50) \times 10^{-21}$ s [24], thus it seems reasonable to globally treat the fission processes as the adiabatic processes. However, in the final stages of the fission process when scission of the neck between the fragments occurs, fission fragments can experience a rapid change in shape and thus trigger the nonadiabatic effects coming from couplings between collective and intrinsic degrees of freedom [25,26]. It is highly desirable to describe this nuclear scission process in a dynamical and nonadiabatic fashion [27], which is crucial to make reliable predictions about the most important properties of fission fragments, such as their intrinsic excitation energies and kinetic energies, their masses, charges, and shapes.

With the rapid development of energy density-functional theory [28–31], nonrelativistic and relativistic microscopic theoretical methods have been used to study the fission paths and dynamics [26,32–45]. Significant progresses have recently been made in the realistic calculation of static potential-energy surface defined in collective space for heavy nuclear fission such as uranium and plutonium. In the dynamic description of the later stages of the fission process, time-dependent density-functional theory (TDDFT) provides a self-consistent, elaborate, and promising microscopic framework because it is a fully microscopic and nonadiabatic method. In this description, the composite fission system smoothly evolves through a mononucleus into the separated fragments and the final properties of fission fragments do not depend on the definition of the scission configuration.

Because the dynamics of the fission process and the influence of shell effects and pairing correlations are considered to be essential assets for describing low-energy fission, microscopic quantum theories are indispensable for a deeper understanding of the fission mechanisms. The dynamic effects near scission have been investigated with the time-dependent Hartree-Fock (TDHF) theory in Refs. [43,46,47]. It is shown that the most of the excitation energy in the fragments is generated in the final stage and that quantum shell effects play a crucial role in the dynamics and formation of the fragments. To consider dynamical pairing correlations, the TDHF theory including BCS dynamical pairing correlations (TD-BCS) [48,49] and the time-dependent superfluid local density approximation (TDSLDA) theory [50,51], which is formally equivalent to the time-dependent Hartree-Fock-Bogoliubov theory (TDHFB), have been applied to fission studies. It is clarified that the most important contributions of pairing to self-consistent mean-field calculations is the ability of the system to allow for level crossings which results in fragments establishing their identity between the saddle and scission

*yansw@bnu.edu.cn

points [4], and that dynamic pairing promotes asymmetric fission to accelerate fragmentation formation [48]. However, it still represents an important challenge to quantitatively understand the individual properties of fission fragments, in particular their excitation energy and their spin, with the microscopic nonadiabatic theory based on time-dependent density-functional theories.

In this paper, a real-space particle- and pairing-density-constrained scheme of TDHFB theory [52], abbreviated rDC-TDHFB in the following, is exploited to study the spontaneous fission process of superfluid nucleus ^{240}Pu. Because the constrained densities in the rDC-TDHFB scheme are the corresponding instantaneous TDHFB densities at every specific time, both the nucleus-nucleus interaction potential and the mass parameter in collective space include the dynamical effects and various excitations described by the particle and pairing densities. Therefore, this method could provide a reliable description of nuclear fission dynamics.

The rDC-TDHFB is implemented by making use of the GOGNY-TDHFB code [53,54] for fission [55]. In our calculation, we formulate RDC-TDHFB numerical scheme into four solvers: (i) The static HFB code to solve the HFB equations for the HFB ground state of a nucleus; (ii) the constrained HFB (CHFB) code to calculate the adiabatic potential in the multidimensional collective space, (iii) the TDHFB code to simulate the nonadiabatic dynamical nuclear processes; and (iv) the RDC-TDHFB code to extract the dynamical potential and other collective variables. In all the solvers, the same parameters of the Gogny D1S effective interaction and the same numerical strategies are used. The detailed information can be found in our previous papers [52,55].

It is remarkable to mention that, in this paper, both the static fission properties by CHFB and the dynamical fission processes by TDHFB and rDC-TDHFB of fissile nucleus are treated in self-consistent ways, and rDC-TDHFB helps us to extract the collective variables including all the dynamics information contained in the one-body particle and pairing density distributions.

II. STATIC AND DYNAMIC DEFORMATION PROPERTIES OF ^{240}Pu

With the aid of our proposed rDC-TDHFB theoretical framework [52], the adiabatic potential of fission nuclei under axial symmetry deformation is calculated, which provides the foundations for subsequent dynamic calculations. Whether the bimodal fission barrier of actinides can be obtained is usually the benchmark for testing theoretical models and calculation codes [56,57]. Considering the abundant experimental and theoretical data available [44,50,51,58–63] and the weak configuration mixing effect [64], the spontaneous fission of ^{240}Pu is studied in this paper.

The parameter set D1S of the Gogny interaction is adopted in this paper. The reaction axis in the z direction is described by the Lagrange mesh method [53,65] with the mesh parameters $N_z = 49$ and $\Delta z = 0.91$ fm. The space of the harmonic-oscillator basis functions with respect to the x and y directions are restricted to $n_x + n_y \leqslant 7$. The parameters of the

deformation harmonic oscillator are given according to

$$\hbar\omega_0 = f\frac{41}{A^{1/3}}\text{MeV}, \quad q = \frac{\omega_\perp}{\omega_z} = 1.43, \quad (1)$$

To obtain a reasonable ground-state energy of HFB, the phenomenological parameter f is introduced, and the recommended value is 1.2 [66]. The initial conditions of TDHFB calculations for dynamical symmetrical and asymmetrical fissions are chosen as the corresponding points to CHFB results as $Q_{20} = 200$ b.

A. Adiabatic potential by constrained Hartree-Fock-Bogoliubov method

To extract the adiabatic potential in static calculations, we use the augmented Lagrange method [67,68] to solve the CHFB equation. The energy density functional is augmented to contain extra terms corresponding to the constraints upon the expectation of the multipole moments $\bar{Q}_{\mu\nu}$,

$$\varepsilon'(q) = \varepsilon(q) - \sum_{\mu\nu} L_{\mu\nu}(\langle Q_{\mu\nu}\rangle - \bar{Q}_{\mu\nu})$$
$$+ \sum_{\mu\nu} C_{\mu\nu}(\langle Q_{\mu\nu}\rangle - \bar{Q}_{\mu\nu})^2, \quad (2)$$

where $\varepsilon(q)$ is mean-field energy, q is short for a number of collective variables, and $\bar{Q}_{\mu\nu}$ are the input parameters and remain constant during the iteration. The $L_{\mu\nu}$ are multipole Lagrange parameters, and the $C_{\mu\nu}$ are stiffness coefficients [69]. The Lagrange parameters $L_{\mu\nu}$ are adjusted step by step in the iterative process in terms of

$$L_{\mu\nu}^{(m+1)} = L_{\mu\nu}^{(m)} - 2C_{\mu\nu}(\langle Q_{\mu\nu}\rangle^{(m)} - \bar{Q}_{\mu\nu}), \quad (3)$$

where $L_{\mu\nu}^{(m)}$ and $\langle Q_{\mu\nu}\rangle^{(m)}$ are $L_{\mu\nu}$ and $\langle Q_{\mu\nu}\rangle$ of the mth iteration, respectively. For the first iteration we have $L_{\mu\nu}^{(0)} = 0$. The detailed description on the numerical algorithm for updating the stiffness coefficients $C_{\mu\nu}$ can be found in Ref. [70].

In this work, the constraints of the quadrupole deformation Q_{20}, triaxiality deformation Q_{22}, and octupole deformation Q_{30} are precisely implemented, while the hexadecapole deformation Q_{40} is free in all fission paths. In addition, the effect of triaxiality Q_{22} significantly reducing first fission barrier to several MeV is also taken into account in the CHFB calculations [44,46,55].

The adiabatic potential $E_{\text{CHFB}}(Q_{20})$ of ^{240}Pu symmetric fission path obtained by the CHFB method is shown in Fig. 1. The two valleys at $Q_{20} = 30$ b and 90 b represent the ground state and isomer state of ^{240}Pu symmetric fission, respectively. The ground-state energy is $E_{\text{g.s.}} = -1794.8$ MeV. The heights of the first and second fission barriers, and the energy of the isomer state with respect to the ground-state energy, are denoted E_A, E_B, and E_{II}, respectively. The values are shown in Table I. Such values are comparable with the results obtained in the previous studies [44,46,61,63] and experimental data [71]. Note that, at the second barrier, there is a long plateau in the $Q_{20} = 130$–200 b range, which is consistent with the results of the relativistic mean-field calculation [45] but does not appear in the Skyrme HFB results in Ref. [44].
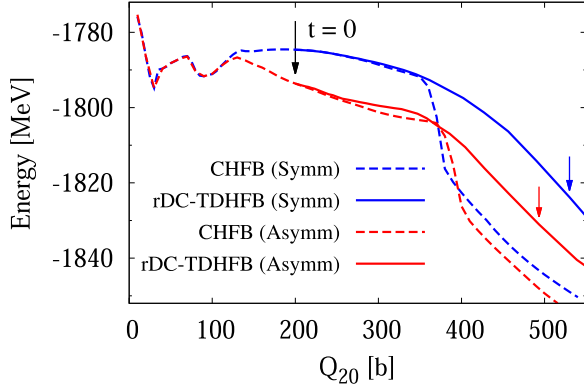
FIG. 1. The adiabatic potential obtained by CHFB method (dashed line) and the dynamical potential by rDC-TDHFB method (solid line) of ^{240}Pu spontaneous fission. The point with a black arrow at $Q_{20} = 200$ b is selected as the initial point of dynamical TDHFB calculation. The red and blue arrows indicate the scission points of dynamical symmetrical and asymmetrical paths, respectively.

Currently, it is still difficult to exactly determine the microscopic fission scission point based on density-functional theory [1]. In this paper, we define the scission point as the minimum density between the fragments along the principal axis of the system is less than 0.05 particles/fm^3, as in Ref. [46]. The particle density in the neck region between the two primary fragments disappears and the nucleon wave function rearranges in the respective fragments, resulting in a sudden drop in the adiabatic potential. In the left panels of Fig. 2(a), we show the profiles of the total density distribution at $Q_{20} = 220, 330, 350, 360, 370, 380$ b in real space for symmetric fission along the adiabatic potential. With a rapid disappearance of the neck, the scission occurs at near 380 b.

To avoid high computational cost, we enter the asymmetric fission path of ^{240}Pu by fixing the elongation $Q_{20} = 200$ b and adding the constraint octupole deformation Q_{30} from 0 to 22.5 b$^{3/2}$. The minimum for exploring adiabatic potential occurs at $Q_{30} = 21.5$ b$^{3/2}$, which is the bottom of the fission valley. And then the octupole constraint is released so that the asymmetric fission path of ^{240}Pu is determined by making small evolutions of the quadrupole constraint from 200 to 0 b and from 200 to 530 b. The resultant potential curve is shown in Fig. 1 as the red dashed line. The ground-state energy of
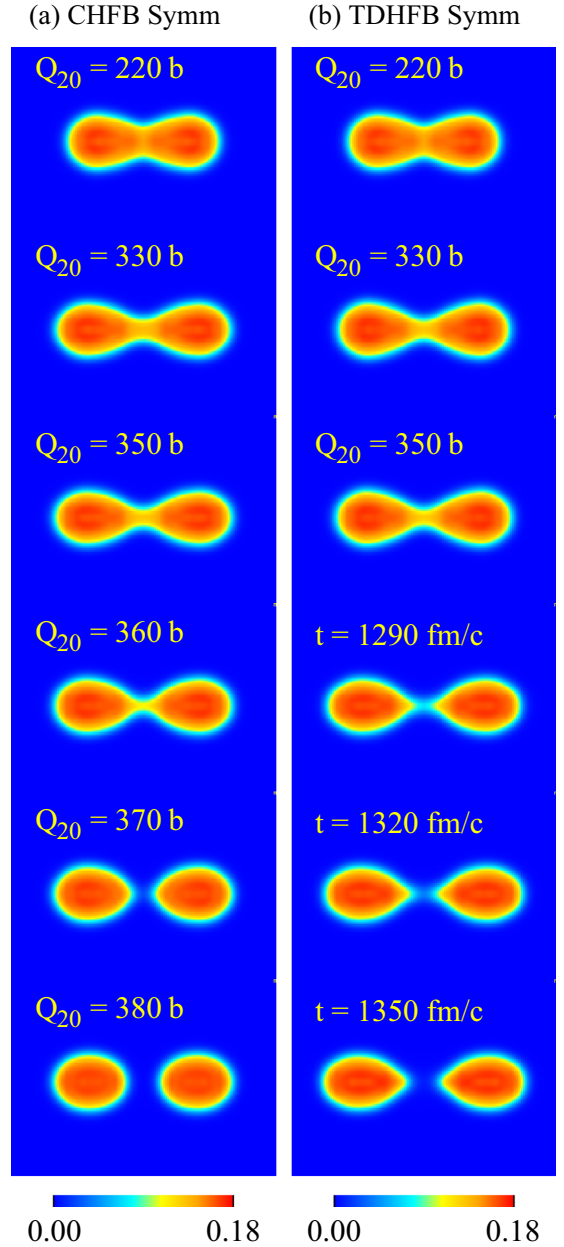

FIG. 2. The profiles of the total density distribution in real space for symmetric fission along (a) adiabatic CHFB path and (b) dynamical TDHFB path.

the asymmetric path is the same as the symmetric path. E_A, E_B and E_{II} values are also shown in Table I. The results are qualitatively consistent with those of Gogny HFB and Skyrme HFB reported in Ref. [44,63]. We can see that the second barrier is significantly lower than that of symmetric path and then the potential descends monotonically until the scission point, indicating that asymmetric fission is more favorable.

The blue dashed lines in Figs. 3 and 4 trace the evolution of octupole deformation Q_{30} and hexadecapole deformation Q_{40} with respect to Q_{20} along the asymmetric path. The step between each cross is 10 b. It is observed that the Q_{30} evolution in asymmetric valleys is almost identical to that of

TABLE I. The obtained energies E_A, E_B, E_{II}, and comparison with the results obtained in the previous studies [44,46,61,63] and experimental data [71].

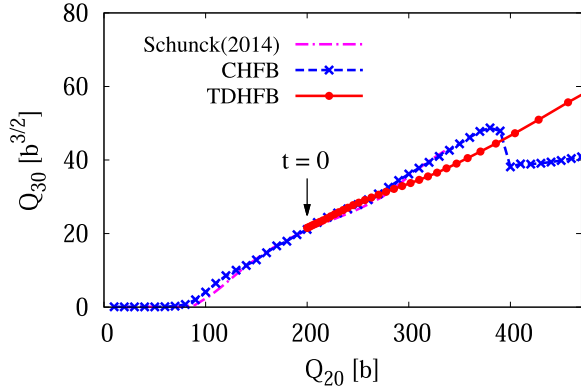| Method	E_A [MeV]	E_B [MeV]	E_{II} [MeV]
This work (Symm)	8.5	10.3	3.1
This work (Asymm)	8.4	8.1	3.1
HFB, Gogny D1M [63]	9.3	8.4	3.1
HFB, Skyrme SkM* [44]	7.64	6.79	2.68
HF + BCS, Skyrme SkM* [46]	8.25	7.68	3.04
HF + BCS, Skyrme SIII [61]	9	13	4
Experiment [71]	6.05	5.15	2.8

FIG. 3. The profiles of octupole deformation Q_{30} along the asymmetric fission path. The results of adiabatic CHFB and dynamical TDHFB calculations compared with the Skyrme HFB result [44].

Skyrme HFB [44]. Since there is no constraint on Q_{40} in our calculation, the deviation from the Skyrme HFB result [44] after 200 b tracks the thinner neck.

It can also be seen from Fig. 1 that the symmetric and asymmetric paths of the fission nuclei from the ground state to the isomer state almost overlap, and the mass asymmetry is mainly formed in the rapid descent of the fission nuclei after passing the second barrier. The scission of the asymmetric adiabatic fission occurs in a larger elongation than that of the symmetric adiabatic fission. In Fig. 5(a), the profiles of the total density distribution at $Q_{20} = 240, 310, 370, 380, 390, 400$ b in real space for asymmetric fission along the adiabatic path shows that the scission occurs at near $Q_{20} = 390$ b.

B. Dynamical potential by rDC-TDHFB method

Considering that the mean-field has no barrier penetration, the initial condition of TDHFB dynamics calculations for symmetric and asymmetric paths is selected by CHFB calculations at elongation $Q_{20} = 200$ b beyond the outer saddle point. This choice of the initial condition should be suited to investigate the role of shell effects at scission. The initial
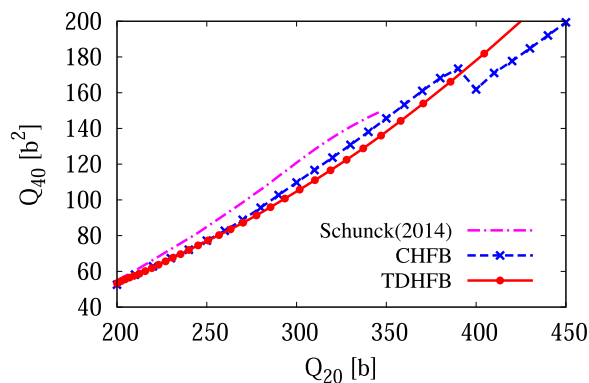

FIG. 4. The evolution of hexadecapole deformation Q_{40} along the asymmetric fission path. The results of adiabatic CHFB and dynamical TDHFB calculations are compared with the Skyrme HFB result [44].
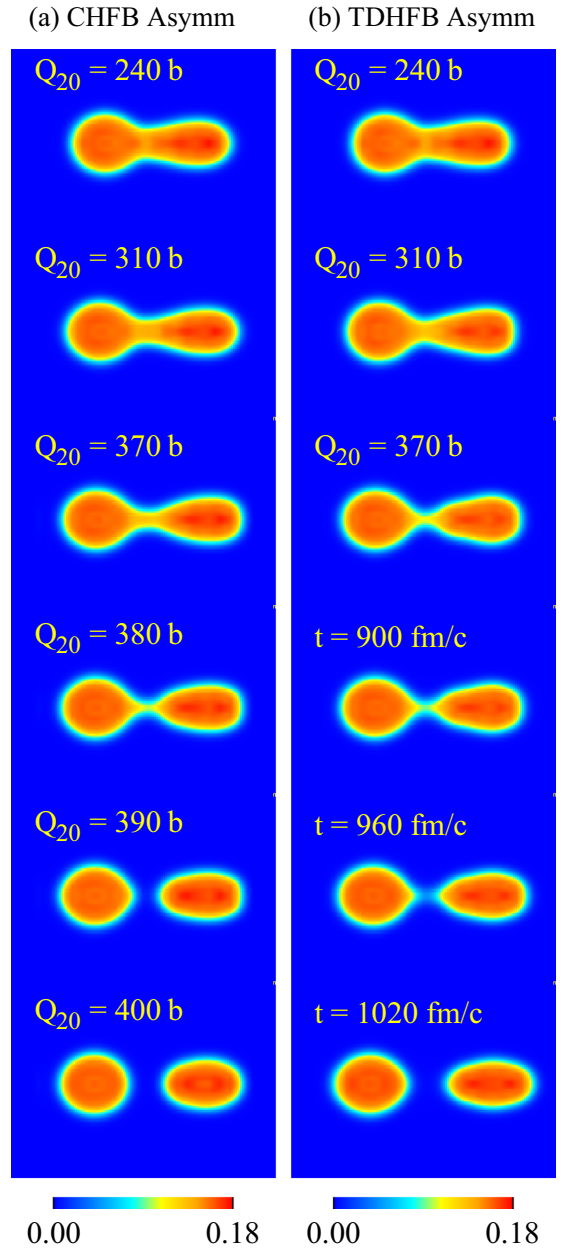

FIG. 5. The profiles of the total density distribution in real space for asymmetric fission along (a) the adiabatic CHFB path and (b) the dynamical TDHFB path.

energy of symmetric path is $E_{\text{TDHFB}} = -1784.6$ MeV, and that of asymmetric path is $E_{\text{TDHFB}} = -1793.6$ MeV. The Gogny D1S effective interaction and all other parameters are exactly the same as ones used in Sec. II A for the CHFB calculation. The time step is set to be $\Delta t = 0.3$ fm/c. We first perform TDHFB simulation and then carry out rDC-TDHFB calculation every 100 steps.

We follow the main procedures proposed in Ref. [52] to implement the density constraints on the TDHFB trajectories to obtain the dynamical potential of ^{240}Pu. In the rDC-TDHFB method, the density-constrained many-body states of a system

are obtained through minimizing

$$\delta\langle\Phi|H - \sum_r \lambda(\boldsymbol{r})[\rho(\boldsymbol{r}) - \rho^{(0)}(\boldsymbol{r}, t)]$$

$$- \sum_r \lambda_{\uparrow\downarrow}^{(2)}(\boldsymbol{r})[\kappa_{\uparrow\downarrow}(\boldsymbol{r}) - \kappa_{\uparrow\downarrow}^{(0)}(\boldsymbol{r}, t)]|\Phi\rangle = 0, \quad (4)$$

with H being the HFB Hamiltonian of the system, $\sigma = \uparrow, \downarrow$ the z projection of the nucleon spin, $\rho^{(0)}(\boldsymbol{r}, t)$ and $\kappa_{\uparrow\downarrow}^{(0)}(\boldsymbol{r}, t)$ the instantaneous TDHFB particle and pairing densities in real space, $\lambda(\boldsymbol{r})$ and $\lambda_{\uparrow\downarrow}^{(2)}(\boldsymbol{r})$ the Lagrange multipliers of the one-body particle and pairing densities, respectively. Consequently, the system goes down to the minimum-energy state described by the HFB state $|\Phi\rangle$ by keeping all the TDHFB dynamical features, such as the one-body particle and pairing density distributions and collective deformation.

After rDC-TDHFB calculations, the density-constrained potential satisfies

$$E_{DC}(q) = \frac{\langle\Phi|H|\Phi\rangle}{\langle\Phi|\Phi\rangle}, \quad (5)$$

with the density-constrained many-body wave function $|\Phi\rangle$ obtained through Eq. (4). Note that, in the realistic implementation of the iteration, the instantaneous TDHFB wave functions are used as the initial iteration wave functions and the iteration process can be accelerated using the modified Broyden's method [72,73].

With the aid of the rDC-TDHFB method, we obtained the dynamical potentials $E_{DC}(Q_{20})$, represented by solid lines in Fig. 1. For symmetric fission, the system takes about 1350 fm/c from the initial state to complete fragmentation and about 1000 fm/c for asymmetric fission. These two timescales are reasonable compared with the results in Refs. [43,49,74,75]. The TDHFB theory realizes the dynamic evolution of all nuclear degrees of freedom without any constraint, so that $E_{DC}(Q_{20})$ changes smoothly when the nucleon rearrangement approaches the scission point and completely separates into two fragments.

For symmetric fission, the dynamical potential and adiabatic potential are close at the beginning of the evolution until the sudden drop in the adiabatic potential, as shown in Fig. 1. Because of the discontinuity of adiabatic potential near the scission point, there is a large discrepancy between the dynamical potential and the adiabatic one. This phenomenon can also be seen in the density-constraint calculation of ^{258}Fm symmetric fission using the HF + BCS method [76]. By comparing $Q_{20} = 220, 330, 350$ b in Figs. 2(a) and 2(b), the evolution of the total density distribution in real space along the dynamical TDHFB path is basically the same as that along the adiabatic CHFB path before the sudden drop. The scission of the TDHFB dynamics occurs near time $t = 1350$ fm/c, corresponding to $Q_{20} = 530$ b [we show the times $t = 1290, 1320, 1350$ fm/c in Fig. 2(b)], which is obviously larger than that of the adiabatic path. The dynamic fragments have a more elongated shape near the scission point, indicating the importance of microscopic dynamic effects.

For asymmetric fission, there is a visible difference between the dynamical potential and adiabatic one before the sudden drop in the adiabatic potential, in Fig. 1. The octupole

TABLE II. The particle numbers of fragments in asymmetric fission by CHFB and TDHFB calculations.

	Z_H	N_H	Z_L	N_L
CHFB	50.90	82.04	43.10	63.96
TDHFB	52.31	82.82	41.69	63.18

deformation Q_{30} and hexadecapole deformation Q_{40} evolution of the dynamical path are shown by the red solid lines in Figs. 3 and 4. From $Q_{20} \approx 260$ b ($t \approx 500$ fm/c), the evolution of Q_{30} and Q_{40} along the dynamical TDHFB path deviates from the adiabatic CHFB path. Compared with adiabatic approximation, this time is too short for the fission system to find the lowest point of the potential-energy surface, revealing a strong nonadiabatic effect during this process. Figure 4 and the comparison of $Q_{20} = 240, 310, 370$ b in Figs. 5(a) and 5(b) further confirm that the evolution of the total density distribution in real space along the dynamical TDHFB path has a thinner neck than that along the adiabatic CHFB path before the sudden drop. The scission point of the TDHFB dynamics occurs near time $t = 1020$ fm/c, corresponding to $Q_{20} = 493$ b [we show the times $t = 900, 960, 1020$ fm/c in Fig. 5(b)].

The difference in the particle number of asymmetric fission fragments between CHFB and TDHFB calculation under the condition of axial symmetric deformation also indicates the nonadiabatic effect. To calculate the particle number of asymmetric fragments, we introduce a section (neck) plane at a point on the z axis of the fissioning nucleus following the separation method in Refs. [77,78]. The section plane is set at the point where the density of the left fragment is equal to the density of the right one. We have to keep in mind that this method may collapse when the overlap of the two subsystems is very large. In such a case, it is unreasonable to separate the highly composite system into two parts. However, in this paper, the TDHFB simulations of fission dynamics are started from the point beyond the outer barrier where the fissioning nucleus is rather largely deformed (i.e., $Q_{20} \approx 200$ b) as shown in Figs. 2 and 5. Therefore, in this paper, the separation method should be reasonable and safe to use.

The resultant proton and neutron numbers of heavy and light fragments (Z_H, Z_L and N_H, N_L) are given in Table II. The heavy fragment of asymmetric fission calculated by adiabatic CHFB method is very close to ^{132}Sn because ^{132}Sn is a doubly magic nucleus. However the fragments obtained by TDHFB dynamics are near to ^{135}Te and ^{105}Mo. The main reason might be that the result of TDHFB depends on the selection of the starting point (between saddle and scission points) of dynamical calculations [79].

The preparation of dynamical potential with multiple dynamic effects facilitates the effective division of internal excitation energy and deformation energy in the fission process and further reveals the properties of fission fragments. This will be further discussed in Sec. IV.

At the end of this section, let us emphasize that the rDC-TDHFB method can help us to calculate the dynamical potential-energy surface and to clarify realistic fission paths,

which include the dynamical effects and various excitations described by TDHFB. Furthermore, there is a consensus that, in the descending stage beyond the saddle point, one can expect nonadiabatic effects due to level crossings. However, to what extent do nonadiabatic effects significantly influence our understanding of the fission dynamics? The study in this section may provides us some enlightenments.

III. ROLES OF PAIRING DYNAMICS

Pairing correlations might play important roles in the dynamics of nuclear deformation [75,80–83]. And fission does not occur on a reasonable timescale in pure TDHF at low energies [47]; adding pairing via TDBCS [48,49] or TDHFB [51] lubricates the dynamics. However, the importance of pairing correlations in the description of fission processes is still not well understood.

In most previous works, the dynamics of fission processes are described with the Skyrme effective nucleon-nucleon interaction (Skyrme-TDHF or Skyrme-TDHFB), within which the isospin-symmetric density-dependent pairing coupling constant

$$g_{\text{eff}}(\boldsymbol{r}) = g\left\{1 - \eta\left[\frac{\rho(\boldsymbol{r})}{\rho_0}\right]\right\} \tag{6}$$

is introduced for the particle-particle channel since the characteristic of zero-range interaction of Skyrme force. $\rho(\boldsymbol{r})$ and ρ_0 are the total and saturation nuclear densities. The extensive phenomenological information gathered so far for ground states of nuclei fails to point to a well-defined value of the parameter η. It has been demonstrated by Ref. [50] that the fission dynamics depends strongly and nonmonotonically on the parameter η. On the top of this, it is also necessary to set an appropriate cutoff energy in the pairing part because the zero-range interaction is assumed in the Skyrme force [84].

In contrast with the Skyrme HFB, in the HFB calculations with the Gogny interaction (Gogny-HFB), the particle-hole channel and the particle-particle channel are treated on an equal footing. In the Gogny-(TD)HFB, a practical cutoff of the energy range of the physical space is introduced naturally from the terms with the Gaussian functions of the Gogny interaction. Therefore, the Gogny interaction is suitable for the formulation of the self-consistent TDHFB framework combined with a practical numerical method for integrating the TDHFB equations [53,55].

To explore the role of pairing dynamics, we first extract the pairing energy

$$E_{\text{pair}} = \frac{1}{4}\sum_{\alpha\beta\gamma\delta}\bar{v}_{\alpha\beta\gamma\delta}\kappa^*_{\alpha\beta}\kappa_{\gamma\delta}, \tag{7}$$

where $\bar{v}_{\alpha\beta\gamma\delta}$ represents the Gaussian part of the two-body matrix elements, and $\kappa_{\alpha\beta}$ is the pairing tensor, respectively. The results for symmetric and asymmetric fission of ^{240}Pu are shown in Figs. 6 and 7. Compare with adiabatic CHFB calculations, the pairing energy of TDHFB is obviously weaker in the whole-mentioned Q_{20} range. The reduction of the pairing correlations in TDHFB calculations results from the internal excitation because level crossings during the dynamic fission are taken into account in TDHFB theory.
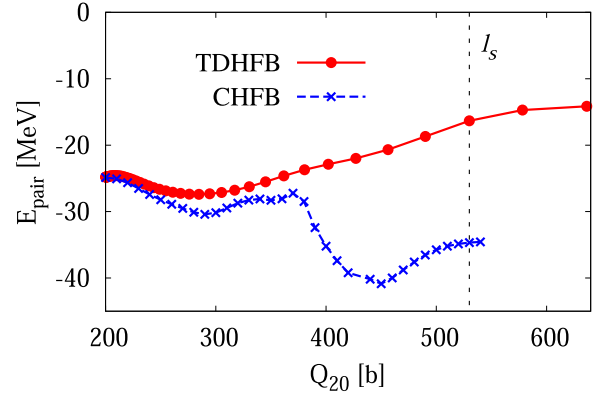

FIG. 6. Pairing energy of the symmetric fission. The vertical dotted line denotes the scission point l_s of dynamical symmetrical fission

We note here that the pairing energy of asymmetric fission with TDHFB does not monotonically change, as shown Fig. 7. The l_1 and l_2 points indicated by the two vertical dotted lines in Fig. 7 are around the scission point of CHFB potential and the dynamical scission point in the asymmetric fission, respectively. At the l_1 and l_2 points, the TDHFB pairing energy is in the large values. We show in the following that this phenomenon is mainly related to the nucleon transfer in asymmetric fission. For the following discussions, it will be convenient to keep in mind that $Q_{20}^{(l_1)}$ of the l_1 point is a little less than the Q_{20} of the scission point in CHFB potential, and the l_2 point corresponds to the dynamical TDHFB scission point exactly, as in Fig. 1.

In heavy-ion fusion reactions, the relation between pairing correlations and multinucleon transfer has been investigated by the TDHF + BCS method with the frozen occupation approximation [85] and the TDHFB theory [86,87]. It is concluded that pairing correlations can effectively enhance two-nucleon transfer in the fusion dynamics. However, in fission dynamics, the relation between pairing correlations
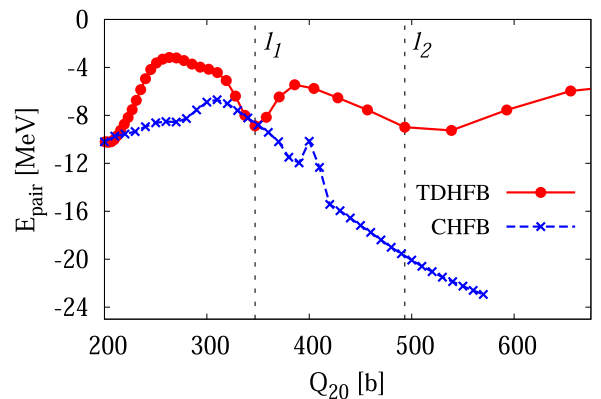

FIG. 7. The same as Fig. 6 but for the ^{240}Pu asymmetric fission path. The l_1 point is around the scission point of the CHFB potential and the l_2 point corresponds to the dynamical scission point in the asymmetric fission, as in Fig. 1. At the l_1 and l_2 points, the TDHFB pairing energy is in the large values.
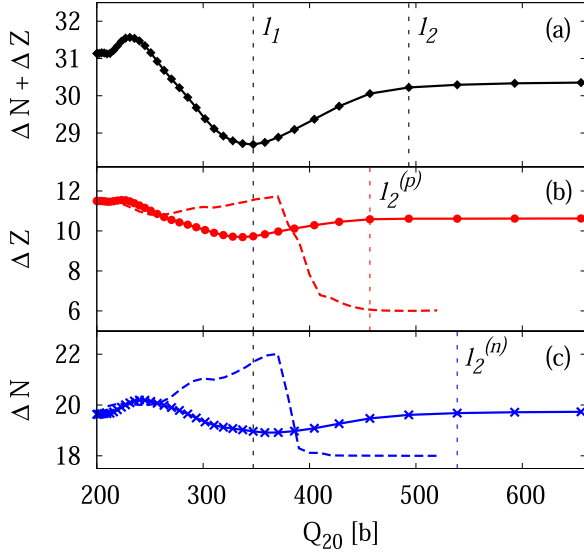
FIG. 8. The evolution of the proton and neutron number differences (a) $\Delta N + \Delta Z$, (b) ΔZ, and (c) ΔN with respect to Q_{20}. The solid-dot lines are of TDHFB and the dashed lines of CHFB. The l_1 and l_2 lines are the same positions as in Fig. 7. The $l_2^{(p)}$ and $l_2^{(n)}$ lines indicate the positions where protons and neutrons stop to transfer in TDHFB, respectively.

FIG. 9. Pairing energy of (a) protons and (b) neutrons of the ^{240}Pu asymmetric fission dynamics. The solid-dot lines are of TD-HFB and the dashed lines of CHFB.

and nucleon transfer is not well understood and is still under investigation.

In the potential curves calculated by CHFB, the symmetric and asymmetric fission paths divide beyond the outer saddle point, say, the descent from saddle to scission. In this dynamical process, the main contributions of pairing to self-consistent mean-field calculations is the ability of the system to allow for level crossings, which break down the adiabatic approximation at level crossing and results in fragments establishing their identity. Therefore, the pairing energy can be considered to play an important role in the odd-even effect of the fission yields and the odd-even effect can be attributed to the pair-breaking effect. Similar to the fusion reactions, the characteristics of pairing energy in Figs. 6 and 7 might be understood from the view of the nucleon transfer effect. With the aid of the neck plane defined in Sec. II B, we calculated the numbers of nucleons transferring between two sides of the neck plane of asymmetric fission dynamics during the descending process from the saddle to scission. The results are given in Fig. 8, where

$$\Delta Z = Z_{\mathrm{H}} - Z_{\mathrm{L}}, \quad \Delta N = N_{\mathrm{H}} - N_{\mathrm{L}}. \tag{8}$$

Z_{H}, Z_{L} and N_{H}, N_{L} are the numbers of protons and neutrons in the heavy and light parts, respectively. $\Delta N + \Delta Z$ in Fig. 8(a) gives the difference in the total number of nucleons between heavy and light fission fragments.

The two extreme points l_1 and l_2 in Fig. 8 correspond to the two valleys of the TDHFB dynamic pairing energy curves in Fig. 7. The $l_2^{(p)}$ and $l_2^{(n)}$ lines indicate the positions where protons and neutrons stop to transfer in TDHFB dynamics, respectively. The result shows a much different picture of nucleon transfer between adiabatic CHFB and dynamic TDHFB
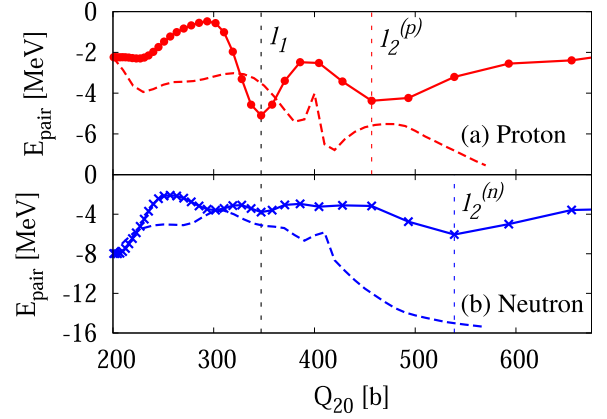
calculations. In the CHFB calculation, from $Q_{20} = 200$ b until the CHFB scission point, neutrons continuously transfer from light fragment to heavy fragment, but protons first transfer from heavy fragment to light fragment and then in the opposite direction. When Q_{20} increases further from the CHFB scission point, a large number of both neutrons and protons suddenly transfers from heavy fragment to light fragment. Finally, both ΔN and ΔZ tend to their constant, unchanging values. The resultant fragments are ^{240}Pu $\rightarrow$ ^{132}Sn $+ ^{108}$Ru. This can be interpreted as an effect of the spherical magic proton shell in tin isotopes.

Now let us see the interesting picture of nucleon transfer in TDHFB calculation. From the initial point ($Q_{20} = 200$ b) of TDHFB to the $l_2^{(p)}$ and/or $l_2^{(n)}$ points, the nucleons are continuously transferred between the heavy and light fragments. Finally, there is one proton transferred from the heavy nucleus to the light nucleus, but no neutron transferred. When Q_{20} is larger than $Q_{20}(l_2^{(p)})$ and/or $Q_{20}(l_2^{(n)})$, there is no nucleon exchanged between heavy and light fragments. The resultant fragments are ^{240}Pu $\rightarrow$ ^{135}Te $+ ^{105}$Mo. Here it might be interesting that $Q_{20}(l_2^{(p)})$ is smaller than $Q_{20}(l_2^{(n)})$.

To understand this phenomenon, we show the evolution of proton and neutron pairing energies along ^{240}Pu asymmetric fission dynamics with respect to Q_{20} in Fig. 9 and the corresponding spin-orbit energies in Fig. 10. There are also much differences of pairing and spin-orbit energies between CHFB and TDHFB calculations. By examining Figs. 8–10, the neutron pairing comes into play earlier, because the existence of the Coulomb barrier makes proton transfer more difficult than neutron. With the dynamic evolution to l_1 line, the number of proton and neutron transfers from the heavy nucleus to light nucleus reaches the maximum, and the proton pairing energy increases significantly while the neutron pairing energy does not. The positions $l_2^{(p)}$ and $l_2^{(n)}$ of proton and neutron fragments separation also surprisingly correspond to valleys of the proton and neutron pairing energies, and asymmetric fission completes the rearrangement of the nucleon number.

In Fig. 10, the CHFB spin-orbit energies of protons and neutrons largely change in the region $Q_{20}(l_2^{(p)}) < Q_{20} <$
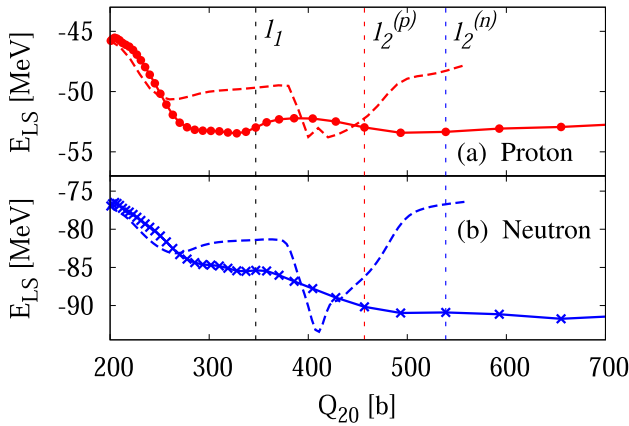
FIG. 10. Spin-orbit energies of (a) protons and (b) neutrons of the ^{240}Pu asymmetric fission dynamics. The solid-dot lines are of TDHFB and the dashed lines of CHFB.

$Q_{20}(l_2^{(n)})$, comparatively, the TDHFB spin-orbit energies change smoothly. This result might be ascribed to the fact that single-particle level crossings are prohibited in the CHFB theory. Due to this restriction, the shell effect in CHFB simulations is much stronger than that in dynamical TDHFB calculations, thus the resultant heavy fragment of asymmetric fission by the adiabatic CHFB method is very close to the magic nucleus.

In the end, there is strong dependence of fission on the dynamics of shell and pairing effects. To obtain the physical insights on the role of multinucleon transfer in fission process, we may need to understand its mechanism more deeply from the microscopic-level dynamics.

IV. FRAGMENTS PROPERTIES

The scission dynamics is arguably one of the least understood processes in fission. A long-term challenge of fission studies is to obtain a more realistic description of the evolution of the fissioning nucleus into fragments, especially in the region where nascent fragments appear near and beyond scission. The time-dependent method should be an ideal tool to study the latter stage of fission, including scission and postscission dynamics, as it is a fully microscopic and nonadiabatic approach [4,5].

In our previous paper [52], we have shown that the rDC-TDHFB could provide a reliable description of nuclear reactions where the pairing effects play one of the central roles in the nuclear property. Because the constrained densities in the rDC-TDHFB scheme are the corresponding instantaneous TDHFB densities at every specific time, both the nucleus-nucleus interaction potential and the mass parameter in collective space include the dynamical effects and various excitations described by the particle and pairing densities.

In this section, with the help of rDC-TDHFB scheme, we extract some collective variables from the results of the microscopic dynamic TDHFB calculations.
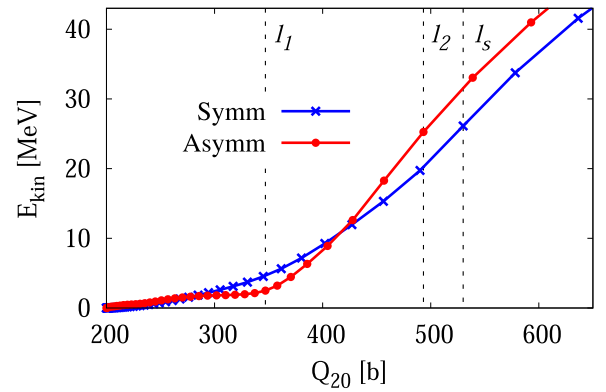

FIG. 11. The collective kinetic energies of the ^{240}Pu symmetric and asymmetric fission paths.

A. Collective kinetic energy

The effective capture of the collective kinetic energy of the fragments is an important step in the microscopic density-functional theory. In principle, the solutions of both TDHF and TDHFB equations satisfy the equation of continuity if the two-body interactions are local [23,88]. In the framework of the TDHFB theory, we adopt the expression of the particle current as

$$\boldsymbol{j}(\boldsymbol{r}) = \frac{1}{2i} \sum_{\alpha\beta} \rho_{\alpha\beta} [\phi_\alpha(\boldsymbol{r}) \vec{\nabla} \phi_\beta^*(\boldsymbol{r}) - \phi_\beta^*(\boldsymbol{r}) \vec{\nabla} \phi_\alpha(\boldsymbol{r})] \delta_{\sigma_\alpha \sigma_\beta}, \quad (9)$$

where the density matrix $\rho_{\alpha\beta}$ is constructed from the V matrix in the TDHFB theory. Note that this particle current, defined by the matrix V, contains all the dynamical effects and the pairing correlations in the sense of the TDHFB theory. The collective kinetic energy of the system can be expressed as

$$E_{\text{kin}} = \frac{\hbar^2}{2m} \int \frac{j^2(\boldsymbol{r})}{\rho(\boldsymbol{r})} d^3 r. \quad (10)$$

Figure 11 shows E_{kin} with respect to Q_{20} of the ^{240}Pu symmetric and asymmetric fission paths. In the process from the initial point of TDHFB dynamics to the l_1 point, the symmetric fission takes 1140 fm/c, while the asymmetric fission takes a little shorter time as 810 fm/c. At the l_1 point, E_{kin} is 4.5 MeV for the symmetric fission, and 2.5 MeV for the asymmetric fission. For symmetric fission, E_{kin} is 26.1 MeV at the l_s point for complete fragmentation. For asymmetric fission, the E_{kin} of the heavy fragment is lower than that of the light fragment. E_{kin} increases monotonically and rapidly in the region after the l_1 point, with a value of 25.2 MeV at the l_2 point. In this case, the values of the heavy and light fragments here are 11.0 and 14.2 MeV, respectively.

The collective kinetic energy E_{kin} in Eq. (10) also can be approximately given in a classical form as follows:

$$E_{\text{kin}} = \tfrac{1}{2} \mu v_{\text{coll}}^2, \quad (11)$$

where μ represents the reduced mass of the fission system. With this approximation, the collective acceleration can be obtained by taking the time derivative on both sides of
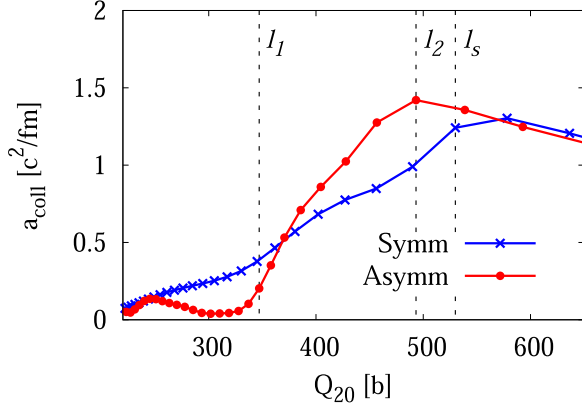
FIG. 12. The collective acceleration of the ^{240}Pu symmetric and asymmetric fission paths. The vertical axis is scaled by a factor of 10^{-4}.

Eq. (11) as

$$a_{\text{coll}} = \frac{1}{\mu v_{\text{coll}}} \frac{dE_{\text{kin}}}{dt}. \tag{12}$$

Here we have ignored the contributions related to the time-dependent effect of the reduced mass μ because our numerical results show that in the descending process, μ slowly changes with respect to time in both symmetric fission and asymmetric fission, and $\frac{1}{2}\frac{d\mu}{dt}v_{\text{coll}}^2$ is several orders of magnitude smaller than $\frac{dE_{\text{kin}}}{dt}$ in the dynamical fission process. The collective acceleration with respect to Q_{20} is shown in Fig. 12. It is clear that the symmetric fission is increasingly accelerated since its acceleration increases smoothly up to the scission l_s point. The asymmetric fission dynamics can be decomposed into three stages. The first stage in $Q_{20} < l_1$ is an extremely slow overdamped process, the second one in $l_1 < Q_{20} < l_2$ is a significantly increasingly acceleration and neck disappears, and, finally, in the third stage $Q_{20} > l_2$, the heavy and light fragments are separated from each other by Coulomb repulsion.

In our calculations, between the initial point of TD-HFB dynamics and l_1 point, the collective speed $v_{\text{coll}}/c \approx$ 0.002–0.004 is very consistent with the values reported in Ref. [51] and significantly smaller than the Fermi velocity $v_F/c \approx 0.25$. The authors of Refs. [50,51] considered this result as the microscopic justification for the assumption of the overdamped Brownian motion model [14] and partially to the scission-point model [89–91], because in both these phenomenological models, it is assumed that the preformed fission fragments are in thermal equilibrium and that the collective energy flow is either vanishing or very small.

However, according to our results in Figs. 11 and 12, the collective kinetic energies of the ^{240}Pu symmetric and asymmetric fission reach $\approx$25 MeV at the scission points l_2 and/or l_s. It is obvious that the nucleus is accelerated in the descent from saddle to scission. In this sense, we think that the assumption of overdamped Brownian motion might be still questionable for symmetric fission and for the second and third stages of the asymmetric fission dynamics.
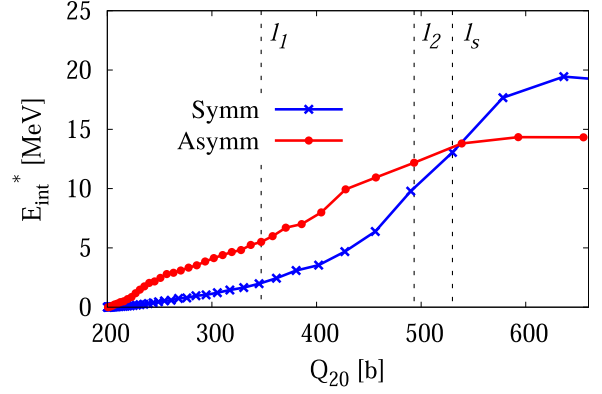

FIG. 13. The internal excitation energy E_{int}^* of the ^{240}Pu symmetric and asymmetric fission paths.

Here, it is worthwhile mentioning that the studies in Refs. [50,51] are based on the TDHFB method as in this paper. The reason why the different collective kinetic energies are obtained, in our understanding at this moment, may result from the different effective nucleon-nucleon interactions that are used in the two simulations, SeaLL1 and SkM* functionals in Refs. [50,51] but Gogny force in our simulation, as mentioned in Sec. III. From a theoretical point of view, it is valuable to leave this subject for the further investigations.

B. Internal excitation energy

In nonadiabatic time-dependent approaches to fission, as TDHFB used in this paper, scission automatically occurs at some time of the time evolution of the compound nucleus as the result of the competition between nuclear and Coulomb forces. Owing to the conservation of total energy in TDHFB, the fragments are automatically in an excited state [1]. Accordingly, the internal excitation energy can be obtained as

$$E_{\text{int}}^* = E_{\text{TDHFB}} - E_{\text{DC}} - E_{\text{kin}}, \tag{13}$$

where the dynamical potential E_{DC} is obtained with the help of the rDC-TDHFB method, and the collective kinetic energy E_{kin} by Eq. (10). The result E_{int}^* is shown in Fig. 13 with respect to the deformation Q_{20} and in Fig. 14 with respect to the evolution time, respectively.

Compared with Fig. 11, it can be seen that the value of E_{kin} is twice as much as that of E_{int}^* near both dynamical scission points l_s and l_2. At the l_1 point, E_{int}^* is 1.9 MeV for symmetric fission and 5.5 MeV for asymmetric fission. It is also clear that most of the internal excitation energy is produced in the extremely large deformation of the fissioning system and in the later stage of the scission process (around the scission point and beyond). A remarkable feature is that, around the dynamical scission point (l_s) of the symmetric fission, E_{pair} changes smoothly and moderately in Fig. 6, however, around both the adiabatic and dynamical scission points (l_1 and l_2 points) of the asymmetric fission, the pairing energy E_{pair} change quickly and reach the maximal values in Fig. 7. This result can serve as the microscopic justification for the nonadiabatic assumption in the scission dynamics beyond the outer barrier. In this dynamic process, the dynamical potential E_{DC}
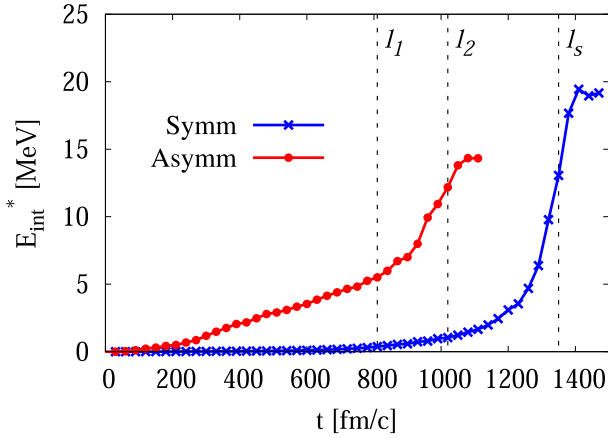
FIG. 14. The internal excitation energy E_{int}^* with respect to time of the ^{240}Pu symmetric and asymmetric fission paths.

quickly goes down (in Fig. 1), the deformed composite system and the nascent fragments are highly excited (in Figs. 13 and 14), and the deformation is accelerated (in Fig. 12).

With the aid of our rDC-TDHFB method, we can extract the excitation energy of the primary fragments. After the two fragments completely separate (beyond the scission) and the nuclear attraction between the fragments vanishes, the conserved energy of the system can be split as

$$E_{\text{TDHFB}} = E[\text{H}] + E[\text{L}] + E_{\text{coul}}, \tag{14}$$

where $E[\text{H}]$ and $E[\text{L}]$ represent the total energy of heavy and light fragments, respectively, E_{coul} is the mutual Coulomb repulsion between two fragments. By performing rDC-TDHFB calculations for each fragment, the dynamical potentials

$$E_{\text{DC}} = E_{\text{DC}}[\text{H}] + E_{\text{DC}}[\text{L}] + E_{\text{coul}} \tag{15}$$

can be obtained after removing the collective kinetic energy and internal excitation energy at the instantaneous TDHFB wave functions. Then, the internal excitation energy of each fragment is calculated as

$$E^*[\text{H/L}] = E[\text{H/L}] - E_{\text{kin}}[\text{H/L}] - E_{\text{DC}}[\text{H/L}], \tag{16}$$

where $E_{\text{kin}}[\text{H/L}]$ represents the collective kinetic energy of the heavy or light fragments. The sum of the internal excitation energies of the heavy and light fragments is numerically equal to the internal excitation energy of the system in Eq. (13) at the same specific time during the TDHFB trajectory.

Our results show that $E^*[\text{H}]$ is smaller than $E^*[\text{L}]$ during the whole evolution process. At the l_2 point in Fig. 13, $E^*[\text{H}]$ is 5.1 MeV and $E^*[\text{L}]$ is 7.1 MeV. The heavy fragment is nearly spherical and has lower excitation energy, while the light fragment is highly deformed and has a higher excitation energy. It is interesting that this result seems to support the conclusion of Ref. [92] but is qualitatively different from previous results reported in Refs. [50,51]. In our understanding, this result is reasonable because the fission process might be an isoentropical rather than isothermal process because the nuclear system may not have sufficient time to thermalize before undergoing fission.

TABLE III. The ground-state energy $E_{\text{g.s.}}$ of TDHFB calculations, the energies E_{DC} of rDC-TDHFB calculations for each fragment and the deformation energy E_{def} at the scission point of ^{240}Pu symmetric and asymmetric fragments. All energies are in MeV.

	Fragment	$E_{\text{g.s.}}$	E_{DC}	E_{def}
Symm	$^{120}_{47}$Ag	−999.7	−989.1	10.6
Asymm	$^{135}_{52}$Te	−1118.8	−1121.2	−2.4
	$^{105}_{42}$Mo	−880.1	−868.6	11.5

C. Deformation energy

The deformation energy of the nascent fragments at the scission point is considered as the main source for the respective excitation in low-energy fission, such as spontaneous or thermal-neutron-induced fission. As fission fragments gradually recover their ground-state deformations, the deformation energy becomes an important part of the available excitation energy and carries an important information on how the fissioning system evolves along the different paths on the potential-energy surface.

In this paper, the deformation energy E_{def} is defined as the difference between E_{DC} of the rDC-TDHFB calculations and the HFB ground-state energy $E_{\text{g.s.}}$ of each fragment. When the rDC-TDHFB scheme is applied to each fragment, all the internal excitation energies are removed and the deformation is preserved at that time. Because the fragments in the two-fragment pathway do not have an integer particle number, as shown in Table II, we applied Gogny-HFB code to deduce the ground states of the fission fragments with the nearest integer particle number (as done in Refs. [46,47,50,51], for example) under the same deformation harmonic-oscillator parameters. The results are presented in Table III. In combination with the real-space total density distributions shown in Figs. 2(b) and 5(b), it is obvious that the resultant fragments of symmetric fission and the light fragment of asymmetric fission have large deformation energy and therefore are largely deformed, while the heavy fragment remains nearly spherical with relatively small deformation energy. This result is reasonable because $^{135}_{52}$Te is close to the doubly magic nucleus ^{132}Sn, but ^{120}Ag and ^{105}Mo are far away.

We should note here that, because our focus in this paper is on the dynamics, we take the mass numbers as the nearest integer to the actual (noninteger) particle numbers for the fission fragments. The code Gogny-HFB has thus been applied to deduce the ground states of the fission fragments to the nearest integer particle number. In this case, $E_{\text{g.s.}}$ and E_{DC} are calculated for different neutron and proton numbers in Table III. This is also the reason $E_{\text{g.s.}} > E_{\text{DC}}$ for fragment $^{135}_{52}$Te. To evaluate E_{def} listed in Table III, it would be instructive to project the individual fragments onto a good particle number [48,93–95].

We have computed the proton number Z and neutron number N distributions of the fragments in Table III by using particle number projection techniques [48,93–95]. As an example, the proton number Z and neutron number N distributions of the heavy fragments ($Z = 52.31$, $N = 82.82$)
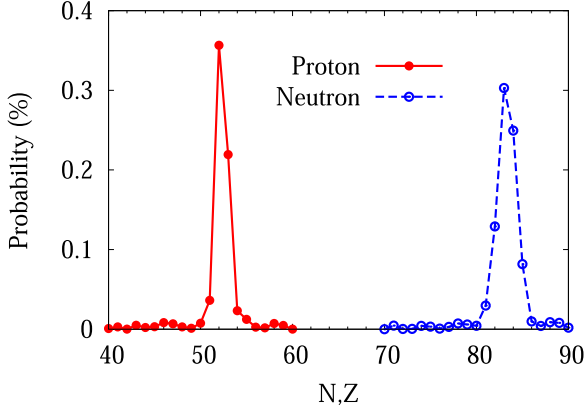
FIG. 15. Proton and neutron number distributions in the fragments.

of ^{240}Pu asymmetric fission are shown in Fig. 15. The most probable heavy fragment is $^{135}_{52}$Te, with the nearest integer particle number to the actual particle numbers of heavy fragment. The other six fragments are $^{136}_{52}$Te, $^{136}_{53}$I, $^{137}_{53}$I, $^{134}_{52}$Te, $^{137}_{52}$Te, $^{135}_{53}$I, in the order of the descending probabilities. The ground-state energies $E_{\text{g.s.}}$ of these six fragments are listed in Table IV. For the heavy fragment of ^{240}Pu asymmetric fission, the ground-state energies of heavy fragments have around ≈ 2 MeV difference when using the nearest integer particle number instead the actual particle numbers of heavy fragments.

D. Total kinetic and excitation energies

Most of the energy released in fission appears in the form of the total kinetic energy (TKE) and total excitation energy (TXE) of the fission fragments. The value of TKE and TXE would significantly influence the multiplicity of evaporated neutrons, particle evaporations, and gamma emissions either before scission or from the separated fragments. Therefore, many efforts have been made to predict the exact values of TKE and TKE, as described in several review articles [1–5]. However, different models predict different values, and it is therefore an important challenge to fission theory to improve the calculations of the collective variables at scission.

With the adiabatic methods, the calculation of TKE strongly depends on the criterion used to define scission configurations and therefore there are large uncertainties of the predicted values of TKE and TXE [36]. But, with the nonadiabatic TDDFT approaches, calculation of TKE and TXE is more rigorously defined since there is no need to characterize scission (the nucleus "automatically" splits as a function of time) and to disentangle the fragments. Under the

help of TDDFT theory, TKE and TXE have been extracted in Ref. [43] with TDHF and in Ref. [51] with TDHFB.

In this paper, with the results of the collective kinetic energy reported in Sec. IV A, we calculated the TKE of ^{240}Pu symmetric and asymmetric fission by summing up the collective kinetic energy and mutual Coulomb repulsion between two fragments when the nuclear attraction between the two fragments vanishes. The result is presented in Table V. The result of our asymmetric fission TKE perfectly agrees with the experimental value 184.8 ± 1.7 MeV obtained by averaging the data sets available in Refs. [58,96,97].

The total excitation energy TXE consists of the following three parts,

$$\text{TXE} = E^*_{\text{adiab}} + E^*_{\text{int}} + E_{\text{def}}, \tag{17}$$

where the adiabatic excitation energy $E^*_{\text{adiab}} = E_{\text{g.s.}} - E_0$ is the energy difference between the ground state of the parent nucleus $E_{\text{g.s.}}$ and the initial state of TDHFB dynamics E_0. The internal excitation energy E^*_{int} and deformation energy E_{def} are given in Secs. IV B and IV C. Compare the calculations in Ref. [43] with TDHF and [51] with TDHFB, calculations of TKE, E^*_{int} and E_{def} in this paper are based on rDC-TDHFB method in a self-consistent way.

We note here that, as shown in Figs. 2 and 5, there are considerable shape elongations of the nascent fragments at scission point calculated by TDHFB dynamics. The associated deformation energy of fragments is included in E_{DC} because E_{DC} is calculated with rDC-TDHFB by constraining the dynamical densities. E^*_{int} defined in Eq. (13) does not include the deformation energy of fragments. Therefore, the deformation energy, which largely contributes to the TXE, has to be considered in Eq. (17) [98,99].

The results of TXE is 24.1 MeV for symmetric fission and 20.1 MeV for asymmetric fission. Such values are very close to the average TXE ≈ 26 MeV expected from empirical arguments in thermal fission of ^{240}Pu [100]. For asymmetric fission, when the excitation energy during the adiabatic process E^*_{adiab} is not considered, the excitation energy of heavy and light fragments derived entirely from nonadiabatic dynamics is 2.7 and 18.6 MeV. This interesting result may help us to elucidate the controversy on the excitation energy sorting mechanism and equilibrium characteristics in superfluid fission dynamics [1,5,92]. To this end, more microscopical TDHFB calculations are needed. We will leave the discussion of this subject to our following presentation.

Finally, we present the main results of this section in Table V. Compare with the relevant works in Refs. [36,51], our predictions of TKE and TXE finely match the experimental data, which might be attributed to the fact that our calculations are based on rDC-TDHFB method in a very self-consistent way.

V. SUMMARY

Nuclear fission is a very complex quantum many-body problem in which all the nucleons are equally involved in the large-amplitude collective dynamics, specially, in the scission process. There is a fundamental relation between the "macroscopic classic" nuclear collective motion and "microscopic

TABLE IV. The ground-state energy $E_{\text{g.s.}}$ of the fragments with good particle numbers

Fragments	$^{136}_{52}$Te	$^{136}_{53}$I	$^{137}_{53}$I	$^{134}_{52}$Te	$^{137}_{52}$Te	$^{135}_{53}$I
$E_{\text{g.s.}}$ (MeV)	-1121.1	-1128.5	-1131.4	-1115.9	-1124.1	-1125.4

TABLE V. The ground-state energy $E_{\text{g.s.}}$ and the initial energy E_{TDHFB} of ^{240}Pu symmetric and asymmetric fission TDHFB dynamics. The adiabatic potential E_{CHFB}, dynamic potential E_{DC}, collective kinetic energy E_{kin}, Coulomb energy E_{coul}, excitation energy during the adiabatic evolution, E^{*}_{adiab}, internal excitation energy E^{*}_{int}, and deformation energy E_{def} at the scission points. The TKE and TXE of both fission paths. All energies are in MeV.

	$E_{\text{g.s.}}$	E_{TDHFB}	E_{CHFB}	E_{DC}	E_{kin}	E_{coul}	E^{*}_{adiab}	E^{*}_{int}	E_{def}	TKE	TXE
Symm	−1794.8	−1784.6	−1848.9	−1823.8	26.1	154.5	−10.2	13.1	21.2	180.6	24.1
Asymm	−1794.8	−1793.6	−1847.5	−1831.0	25.2	158.8	−1.2	12.2	9.1	184.1	20.1

quantum" single-particle effects. To understand the fission dynamics, we have to make classification of how the collective state is realized out of the microscopic single-particle motions.

In this paper, as an effort, a real-space particle- and pairing-density-constrained scheme rDC-TDHFB is used to extract the collective variables from the basic TDHFB calculations. Because the constrained densities in the rDC-TDHFB scheme are the corresponding instantaneous TDHFB densities at every specific time, all the resultant collective variables, such as, energy potential, collective kinetic energy, internal excitation energy and deformation energy of the nascent fragments, etc., include the dynamical effects and various excitations described by the particle and pairing densities. Therefore this method could provide a reliable description of nuclear fissions where the pairing effects play one of the central roles in the nuclear property.

We have applied our proposed rDC-TDHFB scheme to analyze the fission dynamics of actinides nuclei (^{240}Pu, as an example). The energy potential, collective kinetic energy, internal excitation energy, and deformation energy of the nascent fragments are extracted on the basis of the dynam-

ical TDHFB calculations, accordingly. The main results are listed in Table V. It is plausible that our predictions of collective variables, especially the total kinetic energy and total excitation energy of the fission fragments, finely match the experimental data.

However, it is no doubt that even over more than 80 years since the discovery of fission, a full microscopic description remains a challenging subject for modern fission theory and experiment provides often only indirect and hard-to-quantity insights. Many basic questions are still to be answered [1–6]. Among the unclear problems, scission dynamics and the fragments properties should receive much more attention in further studies.

ACKNOWLEDGMENTS

[1] N. Schunck and L. M. Robledo, Rep. Prog. Phys. **79**, 116301 (2016).

[2] A. N. Andreyev, K. Nishio, and K.-H. Schmidt, Rep. Prog. Phys. **81**, 016301 (2018).

[3] K.-H. Schmidt and B. Jurado, Rep. Prog. Phys. **81**, 106301 (2018).

[4] C. Simenel and A. S. Umar, Prog. Part. Nucl. Phys. **103**, 19 (2018).

[5] M. Bender, R. Bernard, G. Bertsch, S. Chiba, J. Dobaczewski, N. Dubray, S. A. Giuliani, K. Hagino, D. Lacroix, Z. Li, P. Magierski, J. Maruhn, W. Nazarewicz, J. Pei, S. Péru, N. Pillet, J. Randrup, D. Regnier, P.-G. Reinhard, L. M. Robledo *et al.*, J. Phys. G **47**, 113002 (2020).

[6] I. Stetcu, A. Bulgac, S. Jin, K. J. Roche, and N. Schunck, EPJ Web Conf. **256**, 00016 (2021).

[7] N. Bohr and J. A. Wheeler, Phys. Rev. **56**, 426 (1939).

[8] P. Möller, D. G. Madland, A. J. Sierk, and A. Iwamoto, Nature (London) **409**, 785 (2001).

[9] P. Möller, A. J. Sierk, T. Ichikawa, A. Iwamoto, R. Bengtsson, H. Uhrenholt, and S. Åberg, Phys. Rev. C **79**, 064304 (2009).

[10] A. Sobiczewski and K. Pomorski, Prog. Part. Nucl. Phys. **58**, 292 (2007).

[11] P. Fröbrich and I. Gontchar, Phys. Rep. **292**, 131 (1998).

[12] Y. Abe, S. Ayik, P.-G. Reinhard, and E. Suraud, Phys. Rep. **275**, 49 (1996).

[13] Z.-H. Liu and J.-D. Bao, Phys. Rev. C **84**, 031602(R) (2011).

[14] J. Randrup and P. Möller, Phys. Rev. Lett. **106**, 132503 (2011).

[15] J. Shen and C. Shen, Sci. China: Phys., Mech. Astron. **57**, 453 (2014).

[16] J. J. Griffin and J. A. Wheeler, Phys. Rev. **108**, 311 (1957).

[17] D. Regnier, N. Dubray, N. Schunck, and M. Verrière, Phys. Rev. C **93**, 054611 (2016).

[18] W. Younes, D. Gogny, and J. Berge, *A Microscopic Theory of Fission Dynamics Based on the Generator Coordinate Method*, Lecture Notes in Physics (Springer, 2019), Vol. 950.

[19] M. Verriere and D. Regnier, Front. Phys. **8**, 233 (2020).

[20] M. Baranger, J. Phys., Colloq. **33**, C5-61 (1972).

[21] M. Baranger and M. Vénéroni, Ann. Phys. (NY) **114**, 123 (1978).

[22] F. Villars, Nucl. Phys. A **285**, 269 (1977).

[23] P. Ring and P. Schuck, *The Nuclear Many-Body Problem* (Springer-Verlag, New York, 1980).

[24] D. J. Hinde, D. Hilscher, H. Rossner, B. Gebauer, M. Lehmann, and M. Wilpert, Phys. Rev. C **45**, 1229 (1992).

[25] M. Rizea and N. Carjan, Nucl. Phys. A **909**, 50 (2013).

[26] N. Dubray, H. Goutte, and J.-P. Delaroche, Phys. Rev. C **77**, 014310 (2008).

[27] A. S. Umar, V. E. Oberacker, J. A. Maruhn, and P.-G. Reinhard, J. Phys. G **37**, 064037 (2010).

[28] M. Samyn, S. Goriely, and J. M. Pearson, Phys. Rev. C **72**, 044316 (2005).

[29] T. Bürvenich, M. Bender, J. A. Maruhn, and P.-G. Reinhard, Phys. Rev. C **69**, 014307 (2004).

[30] S. Karatzikos, A. Afanasjev, G. Lalazissis, and P. Ring, Phys. Lett. B **689**, 72 (2010).

[31] H. Abusara, A. V. Afanasjev, and P. Ring, Phys. Rev. C **82**, 044303 (2010).

[32] H. Goutte, J. F. Berger, P. Casoli, and D. Gogny, Phys. Rev. C **71**, 024316 (2005).

[33] L. Bonneau, Phys. Rev. C **74**, 014301 (2006).

[34] A. Staszczak, A. Baran, J. Dobaczewski, and W. Nazarewicz, Phys. Rev. C **80**, 014309 (2009).

[35] J. C. Pei, W. Nazarewicz, J. A. Sheikh, and A. K. Kerman, Phys. Rev. Lett. **102**, 192501 (2009).

[36] W. Younes and D. Gogny, Phys. Rev. Lett. **107**, 132501 (2011).

[37] M. Warda and J. L. Egido, Phys. Rev. C **86**, 014322 (2012).

[38] H. Abusara, A. V. Afanasjev, and P. Ring, Phys. Rev. C **85**, 024314 (2012).

[39] M. Mirea, Phys. Lett. B **717**, 252 (2012).

[40] A. Staszczak, A. Baran, and W. Nazarewicz, Phys. Rev. C **87**, 024320 (2013).

[41] J. D. McDonnell, W. Nazarewicz, and J. A. Sheikh, Phys. Rev. C **87**, 054327 (2013).

[42] J. Sadhukhan, K. Mazurek, A. Baran, J. Dobaczewski, W. Nazarewicz, and J. A. Sheikh, Phys. Rev. C **88**, 064314 (2013).

[43] C. Simenel and A. S. Umar, Phys. Rev. C **89**, 031601(R) (2014).

[44] N. Schunck, D. Duke, H. Carr, and A. Knoll, Phys. Rev. C **90**, 054305 (2014).

[45] B.-N. Lu, E.-G. Zhao, and S.-G. Zhou, Phys. Rev. C **85**, 011301(R) (2012).

[46] P. Goddard, P. Stevenson, and A. Rios, Phys. Rev. C **92**, 054610 (2015).

[47] P. Goddard, P. Stevenson, and A. Rios, Phys. Rev. C **93**, 014620 (2016).

[48] G. Scamps, C. Simenel, and D. Lacroix, Phys. Rev. C **92**, 011602(R) (2015).

[49] G. Scamps and C. Simenel, Nature (London) **564**, 382 (2018).

[50] A. Bulgac, P. Magierski, K. J. Roche, and I. Stetcu, Phys. Rev. Lett. **116**, 122504 (2016).

[51] A. Bulgac, S. Jin, K. J. Roche, N. Schunck, and I. Stetcu, Phys. Rev. C **100**, 034615 (2019).

[52] L. Tong and S. Yan, Phys. Rev. C **105**, 014613 (2022).

[53] Y. Hashimoto, Phys. Rev. C **88**, 034307 (2013).

[54] G. Scamps and Y. Hashimoto, Phys. Rev. C **100**, 024623 (2019).

[55] L. Tong, Y. Hashimoto, and S. Yan, Kexue Tongbao (Chin. Ed.) **65**, 2225 (2020).

[56] J. Stone and P.-G. Reinhard, Prog. Part. Nucl. Phys. **58**, 587 (2007).

[57] G. F. Bertsch, W. Loveland, W. Nazarewicz, and P. Talou, J. Phys. G. **42**, 077001 (2015).

[58] C. Wagemans, E. Allaert, A. Deruytter, R. Barthélémy, and P. Schillebeeckx, Phys. Rev. C **30**, 218 (1984).

[59] J. Toraskar and E. Melkonian, Phys. Rev. C **4**, 1391 (1971).

[60] D. E. Watt, F. J. Bannister, J. B. Laidler, and F. Brown, Phys. Rev. **126**, 264 (1962).

[61] H. Flocard, P. Quentin, D. Vautherin, M. Veneroni, and A. Kerman, Nucl. Phys. A **231**, 176 (1974).

[62] V. Strutinsky, Nucl. Phys. A **95**, 420 (1967).

[63] R. Rodríguez-Guzmán and L. M. Robledo, Eur. Phys. J. A **50**, 142 (2014).

[64] M. Bender, P.-H. Heenen, and P. Bonche, Phys. Rev. C **70**, 054304 (2004).

[65] D. Baye, Phys. Rep. **565**, 1 (2015).

[66] J. Dudek, Z. Szymański, and T. Werner, Phys. Rev. C **23**, 920 (1981).

[67] M. R. Hestenes, J. Optim. Theory Appl. **4**, 303 (1969).

[68] A. Staszczak, M. Stoitsov, A. Baran, and W. Nazarewicz, Eur. Phys. J. A **46**, 85 (2010).

[69] J. Dobaczewski and J. Dudek, Comput. Phys. Commun. **102**, 166 (1997).

[70] J. Nocedal and S. Wright, *Numerical Optimization*, Springer Series in Operations Research and Financial Engineering (Springer, New York, 2006).

[71] R. Capote, M. Herman, P. Obložinský, P. Young, S. Goriely, T. Belgya, A. Ignatyuk, A. Koning, S. Hilaire, V. Plujko, M. Avrigeanu, O. Bersillon, M. Chadwick, T. Fukahori, Z. Ge, Y. Han, S. Kailas, J. Kopecky, V. Maslov, G. Reffo *et al.*, Nucl. Data Sheets **110**, 3107 (2009).

[72] D. D. Johnson, Phys. Rev. B **38**, 12807 (1988).

[73] A. Baran, A. Bulgac, M. M. Forbes, G. Hagen, W. Nazarewicz, N. Schunck, and M. V. Stoitsov, Phys. Rev. C **78**, 014318 (2008).

[74] K. T. R. Davies, A. J. Sierk, and J. R. Nix, Phys. Rev. C **13**, 2385 (1976).

[75] J. W. Negele, S. E. Koonin, P. Möller, J. R. Nix, and A. J. Sierk, Phys. Rev. C **17**, 1098 (1978).

[76] Y. Qiang and J. C. Pei, Phys. Rev. C **104**, 054604 (2021).

[77] K. Washiyama and D. Lacroix, Phys. Rev. C **78**, 024610 (2008).

[78] R. Keser, A. S. Umar, and V. E. Oberacker, Phys. Rev. C **85**, 044606 (2012).

[79] Y. Tanimura, D. Lacroix, and S. Ayik, Phys. Rev. Lett. **118**, 152501 (2017).

[80] F. Barranco, G. F. Bertsch, R. A. Broglia, and E. Vigezzi, Nucl. Phys. A **512**, 253 (1990).

[81] G. F. Bertsch, Nucl. Phys. A **574**, 169 (1994).

[82] A. Bohr, B. R. Mottelson, and D. Pines, Phys. Rev. **110**, 936 (1958).

[83] G. F. Bertsch and A. Bulgac, Phys. Rev. Lett. **79**, 3539 (1997).

[84] P. J. Borycki, J. Dobaczewski, W. Nazarewicz, and M. V. Stoitsov, Phys. Rev. C **73**, 044319 (2006).

[85] G. Scamps and D. Lacroix, Phys. Rev. C **87**, 014605 (2013).

[86] S. Ebata and T. Nakatsukasa, JPS Conf. Proc. **1**, 013038 (2014).

[87] Y. Hashimoto and G. Scamps, Phys. Rev. C **94**, 014610 (2016).

[88] J.-P. Blaizot and G. Ripka, *Quantum Theory of Finite Systems* (MIT Press, Cambridge, 1985).

[89] B. D. Wilkins and E. P. Steinberg, Phys. Lett. B **42**, 141 (1972).

[90] B. D. Wilkins, E. P. Steinberg, and R. R. Chasman, Phys. Rev. C **14**, 1832 (1976).

[91] J.-F. Lemaître, S. Panebianco, J.-L. Sida, S. Hilaire, and S. Heinrich, Phys. Rev. C **92**, 034617 (2015).

[92] K.-H. Schmidt and B. Jurado, Phys. Rev. Lett. **104**, 212501 (2010).

[93] C. Simenel, Phys. Rev. Lett. **105**, 192701 (2010).

[94] M. Verriere, N. Schunck, and T. Kawano, Phys. Rev. C **100**, 024612 (2019).

[95] A. Bulgac, Phys. Rev. C **100**, 034612 (2019).

[96] K. Nishio, Y. Nakagome, I. Kanno, and I. Kimura, J. Nucl. Sci. Technol. (Abingdon, UK) **32**, 404 (1995).

[97] C. Tsuchiya, Y. Nakagome, H. Yamana, H. Moriyama, K. Nishio, I. Kanno, K. Shin, and I. Kimura, J. Nucl. Sci. Technol. (Abingdon, UK) **37**, 941 (2000).

[98] C. Morariu, A. Tudora, F.-J. Hambsch, S. Oberstedt, and C. Manailescu, J. Phys. G **39**, 055103 (2012).

[99] K.-H. Schmidt and B. Jurado, Phys. Rev. C **83**, 061601(R) (2011).

[100] D. G. Madland, Nucl. Phys. A **772**, 113 (2006).